Robust 3D Face Landmark Localization based on Local Coordinate Coding

Mingli Song, *Senior Member, IEEE,* Dacheng Tao, *Senior Member, IEEE,* Shengpeng Sun, Chun Chen, and Stephen J. Maybank *Fellow, IEEE,*

***Abstract*—In the 3D facial animation and synthesis community, input faces are usually required to be labeled by a set of landmarks for parameterization. Because of the variations in pose, expression and resolution, automatic 3D face landmark localization remains a challenge. In this paper, a novel landmark localization approach is presented. The approach is based on Local Coordinate Coding (LCC) and consists of two stages. In the first stage, we perform nose detection, relying on the fact that the nose shape is usually invariant under the variations in the pose, expression and resolution. Then, we use the Iterative Closest Points (ICP) algorithm to find a 3D affine transformation that aligns the input face to a reference face. In the second stage, we perform re-sampling to build correspondences between the input 3D face and the training faces. Then, an LCC-based localization algorithm is proposed to obtain the positions of the landmarks in the input face. Experimental results show that the proposed method is comparable to state of the art methods in terms of its robustness, flexibility and accuracy.**

***Index Terms*—Landmark, 3D Affine Transformation, Face Alignment, Face Re-sampling, Iterative Closest Points, Local Coordinate Coding.**

I. Introduction

THREE-dimensional (3D) faces have been widely used in many applications in computer vision, computer graphics and virtual reality. With the development of scanning technology, large numbers of 3D coordinates can be obtained by 3D scanning devices, such as laser scanners, structured light scanners and other devices, in a very short time. Due to the limitation of the scanning devices, the 3D face data, which are usually in the form of point clouds, are acquired from different distances, orientations and expressions, which leads to enormous variations in the pose, face deformation, resolution, and even facial area. To build correspondences between the 3D faces that have different resolutions, poses, expressions and facial areas, many computer graphics and computer vision applications require corresponding landmarks for 3D face parameterization, which is the basis of further manipulation such as expressive analogy and animation. The landmarks are a set of 3D locations in a 3D face that are positioned to describe and parameterize the shape and semantics of the 3D faces.

Many 3D face applications [30], [44] locate the landmarks manually by using interactive tools, which is straightforward yet time consuming. Fortunately, a variety of methods for 3D face landmark localization have been proposed in recent years. These methods are divided into two groups: feature detection-based methods and statistical point distribution model (PDM)-based methods.

A. Feature Detection-based Approach

In the feature detection-based methods, the landmarks are defined by significant features, such as nose tip, nose wing, eye corners and mouth corners. These features are easily modeled by local descriptors. Lu *et al.* [1] proposed an algorithm to detect the nose tip on a rotated 3D face and to correct the facial pose by angle space quantization. However, this algorithm is based on the hypothesis that the nose tip on a frontal face is the closest point to the scanner. However, this hypothesis is not tenable in many cases. In addition, this method is computationally expensive when the angle space quantization is fine grained. Similar methods have been proposed by Perakis *et al.* [3] to automatically detect the nose. In [3], the face pose is aligned by Procrustes analysis in which the candidate nose points are extracted based on the curvature information, and the mean shape is used to compute the rigid transformation. The candidate points that have a minimum Procrustes distance are regarded as nose points.

Many curvature-based methods have also been proposed to detect the nose tip [5]–[7]. The shape index [8] is used by Colbry *et al.* in which a statistical model is used to identify the nose position. Lin [6] uses principle curvatures and combines 2D and 3D data to describe the face. A search is conducted along the normal directions from the boundaries of the eyes to find the nose tip. Segundo *et al*. [7] proposed a method to detect the nose tip by combining traditional image segmentation techniques and an adapted method for 2D facial feature extraction with the curvature information. All of these nose detection methods produce good results for frontal faces but have limited capabilities for faces that are in arbitrary poses.

Mian *et al.* [9] proposed a coarse-to-fine approach for detecting the nose tip by horizontally slicing the 3D face at multiple steps. A candidate point is selected on each slice.

Manuscript received January 18, 2013; revised August 5, 2014; accepted September 24, 2014. This work was supported in part by the National Natural Science Foundation of China under Grant 61170142, by the the Program of International S&T Cooperation (2013DFG12840), National High Technology Research and Development Program of China (2013AA040601), and by Australian Research Council Projects DP-140102164 and FT-130101457.

M. Song S. Sun, and C. Chen are with the College of Computer Science, Zhejiang University, Hangzhou 310027, China.

D. Tao is with the Centre for Quantum Computation & Intelligent Systems and the Faculty of Engineering and Information Technology, University of Technology, Sydney, 235 Jones Street, Ultimo, NSW 2007, Australia (email: dacheng.tao@uts.edu.au).

S. J. Maybank is with the Department of Computer Science and Information Systems, Birkbeck College, University of London

Only the points that correspond to the nose ridge should form a line in the *x*-*y* plane. However, this approach requires a near-frontal face. Dibeklioğlu *et al.* [11] introduced a statistical method and a heuristic method for nose tip detection. The statistical method is based on an analysis of local features using the depth map and the gradient information of the depth map. The heuristic method locates the nose tip utilizing curvature values to address the pose variations. However, the statistical method cannot handle 3D faces that have pose variations, and the heuristic method is inaccurate on the 3D faces that have a yaw rotation that is greater than 45 degrees. Romero-Huertas *et al.* [12] used a graph model to locate the inner eye corners and the nose tip simultaneously. A graph matching algorithm is based on a distance-to-local plane node property and a Euclidean distance arc property. The feature combination that has the minimum Mahalanobis distance is selected. However, this method is sensitive to changes in the scale and radius of the distance-to-local plane.

Creusot *et al.* presented a multimodal feature point localization approach [14]. In [14], multiple local surface descriptors are used to extract interesting points of specific salient shapes first. Then, a model-fitting operation is exploited to select the facial feature points from the extracted interesting points. In the meantime, Fanelli *et al.* [15] developed a random forest-based facial feature detection system, in which a set of fixed-sized patches were extracted to vote for each of the salient feature points, e.g., eye corners, mouth corners and chin tip. The random forest-based facial feature point detection system can robustly and accurately locate the feature points on the 3D face sequence in real time.

It is noticeable that all of the above-mentioned methods align the face by relying on one vertex or a few reliable vertices, such as the nose tip and the eye corners. However, it is known that in many applications (e.g., face animation, parameterization, synthesis), the landmarks are required to be located at the forehead, cheeks, side of the face and other specific positions. It remains challenging to find reliable landmarks in those areas of the face that do not appear to have any significant features.

B. Statistical Point Distribution Model-based Approach

In 1995, Cootes and Taylor [13] proposed an Active Shape Model (ASM) to locate objects in images. Then, an Active Appearance Model (AAM) [17]–[23] was developed for face landmark detection. Recently, AAM has been extended to 3D face modeling [24]–[26]. Although these algorithms can detect a set of landmarks by fitting an AAM to an image, 2D image or 3D texture information is required. These algorithms are not suitable if the data consist of only a 3D point cloud or a triangulated face mesh.

Nair *et al.* [4] presented a 3D face landmark localization method that was based on a point distribution model (PDM). The PDM is a statistical model that describes the relative positions of the landmarks. The learned PDM is used to fit the 3D face using a transformation between the model points and the candidate vertices on the mesh. The landmarks defined in the PDM include not only the eye and mouth corners and the nose and chin tips but also the eyebrows. However, the PDM is sensitive to variations in expression and to incomplete coverage of the 3D face. Afterward, Perakis *et al.* [10] introduced a 3D facial landmark localization method that was robust to yaw and expression changes. In [10], the shape index and spin image are used as features for detecting candidate landmarks e.g., eye corners, mouth corners, and nose tip. Then, a pre-trained PDM is explored to filter the landmarks.

To overcome the limitation of [15], Fanelli *et al.* further built a random forest based AAM (RF-AMM) [16] to locate more landmarks robustly, in which the random forest based pose estimation [15] is used to accomplish the initialization. RF-AAM achieves real-time performance and high accuracy against variations in expression and head pose. However, it is noticeable that both the random forest in [15] and the RF-AAM in [16] require that the testing data have a similar resolution to the training data.

In this paper, we propose a new framework for 3D face landmark localization that is based on local coordinate coding, which enables us to locate landmarks robustly under variations in pose, expression and resolution and even in cases when the 3D face is not completely covered by the data. Our approach consists of two stages. In the first stage, 3D face alignment is performed based on nose detection. Our nose detection is different from all of the methods mentioned above in that the whole nose region is detected including the bridge and the sides of the nose. After nose detection, we apply an affine transform to obtain a coarse alignment between the 3D face and a reference 3D face. Then, an ICP algorithm [2] is employed to refine the alignment. In the second stage, we first perform 3D face re-sampling to build the training database for LCC-based [27] landmark localization. Then, a coupled dictionary is learned based on the training database and the corresponding landmarks. Afterwards, given a new 3D face, a set of landmarks are synthesized based on the coupled dictionary. Finally, the landmarks are located under the guidance of synthesized landmarks that are based on the coupled dictionary.

The remainder of this paper is organized as follows. Section II describes the 3D face alignment that is based on nose detection. Section III describes the 3D face landmark localization that is based on LCC. Section IV presents the experimental results. Finally, Section V summarizes our method and proposes future directions for further research.

II. Stage One: Coarse Alignment

In this section, we describe in detail our proposed 3D face alignment method, which is based on nose detection. The 3D face alignment is accomplished through an ICP algorithm that is based on the detected nose. There are three advantages to base the 3D face alignment on the nose. First, the nose is at the center of the face, and thus, it is likely to be included in the scanned data. If the nose is omitted from the scanned data, then the data are unlikely to be useful for applications such as computer animation, games and movie production. Second, it is obvious that the nose is the most distinctive feature

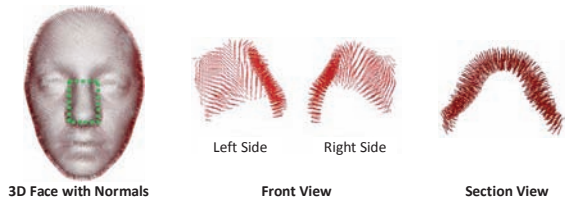

Fig. 1. (a) 3D Face with normals. (b) Front view of the nose with normals. (c) Section view of the nose with normals.

of the face, and it is easy to detect. Third, the nose is the most stable feature of the face; in particular, the shape of the nose is invariant under variations in the pose, resolution and expression. It might be argued that the forehead is also stable; however, the forehead lacks distinctive features. In addition, the area of the forehead that is included in a scan varies from one scan to another.

A. Nose Detection

The proposed approach detects the nose region by partitioning the input 3D face into several patches, in such a way that the vertices in the same patch have similar geometric properties. Because of to the distinct shape of the nose, the vertices on the nose will be assigned to one of two patches on either side of the nose. A spin-image-based descriptor is used to represent each patch in the face, and a trained SVM detector is then used to select the two patches on either side of the nose. In this way, the whole nose is obtained.

1) Preliminary: The input to our method is an arbitrary-pose 3D face that is described by a set of 3D vertices and triangles. However, these vertices and triangles alone are not sufficient for nose detection: the vertex normals are necessary. A vertex normal is a surface normal vector that is located at a 3D vertex that is included in the data. Several algorithms for computing vertex normals have been proposed in recent decades [38]. In this paper, the vertex normal is calculated by a very simple algorithm, which is defined as follows:

$$n_p = \frac{1}{m}\sum_{i=1}^{m} N_i \tag{1}$$

where the summation is over all of the facets that are incident to the vertex p, and N_i is the normal vector to the plane that contains the i-th triangular facet.

Fig. 1.(a) shows a 3D face that has all of the vertex normals, and (b) and (c) are a front view and section view, respectively, of the nose with vertex normals. As Fig. 1 shows, the vertex normals on the same side of the nose share similar directions, while the vertex normals on different sides of the nose are nearly symmetric and have different directions. This circumstance is a very distinguishing characteristic that is used by us to differentiate the vertices on the nose from the vertices on other parts of the 3D face.

2) Face Partitioning: Next, we explain in detail how to partition a 3D face into several patches based on the vertex normals. This partitioning is performed in two steps: clustering and graph-based partitioning.

Step 1. **Clustering**. When considering that each vertex normal is computed using the data in a local neighborhood that is independent of the face pose, we perform clustering that is based on the directions of the vertex normals. We use k-means clustering [39] to obtain a cluster set $C = \{c_1, c_2, c_3, \cdots, c_k\}$. Figs. 2.(a), 3.(a) and 4.(a) show our results on different 3D face databases. The k value of the k-means clustering is set to 15 empirically.

From the figures, we observe that the vertices on a given side of the nose are assigned to the same cluster, as we would expect. This result is crucial because the nose is detected by finding the specific clusters on its two sides. However, note that some vertices from other regions of the face (e.g., a cheek) are assigned to the same cluster as the nose vertices. In addition, there are many small clusters that have only a few vertices. These problems make it difficult to detect the nose. For better detection, a graph-based partitioning algorithm is used to edit the clusters that are obtained using the k-means algorithm.

Algorithm 1 Graph-based Partitioning Algorithm

Input: Face mesh $F =< V, E >$,
Cluster set $C = \{c_1, c_2, c_3, \cdots, c_k\}$,
Edge weight list $W = \{w_1, w_2, w_3, \cdots, w_m\}$,
Minimum patch size threshold λ.
Output: Patch set $P = \{p_1, p_2, p_3, \cdots, p_n\}$

```
begin
    P = {}
    for i = 1 → k do begin
        Divide c_i into patches based on the connectivity and obtain
        the patch set P_i  P = P_i ∪ P
    end for
    for t = 1 → m do begin
        Get the edge e_ij = (v_i, v_j) according to the weight w_t
        Find patch p_i and patch p_j, where v_i ∈ p_i and v_j ∈ p_j
        if p_i ≠ p_j and min(size(p_i), size(p_j)) < λ
            Merge p_i with p_j and update P
        else
            Continue
        end if
    end for
    return P = {p_1, p_2, p_3, ··· , p_n}
end
```

Step 2. **Graph-based Partitioning**. The graph-based partitioning algorithm merges small clusters. Let $F = (V, E)$ denote a 3D face mesh that has a set of vertices V and a set of undirected edges E. Each edge $e_{ij} \in E$ is a pair of adjacent vertices (v_i, v_j) that has a corresponding weight $w(e_{ij})$, where $v_i, v_j \in V$. The edge weight is a measure of the distance between two adjacent vertices. The weight of an edge that connects two adjacent vertices from the same cluster is zero. For an edge e_{ij} that connects two adjacent vertices from different clusters, the weight is calculated as follows:

$$w(e_{ij}) = e^{-\cos\theta} \tag{2}$$

where θ is the angle between the normal vectors v_i and v_j. A larger angle yields a larger value for the weight. Considering we have

$$\cos\theta = \frac{n_i \cdot n_j}{|n_i||n_j|} \tag{3}$$

where n_i and n_j are unit normal vectors of v_i and v_j, and $|n_i||n_j| = 1$, the weight function can be rewritten as

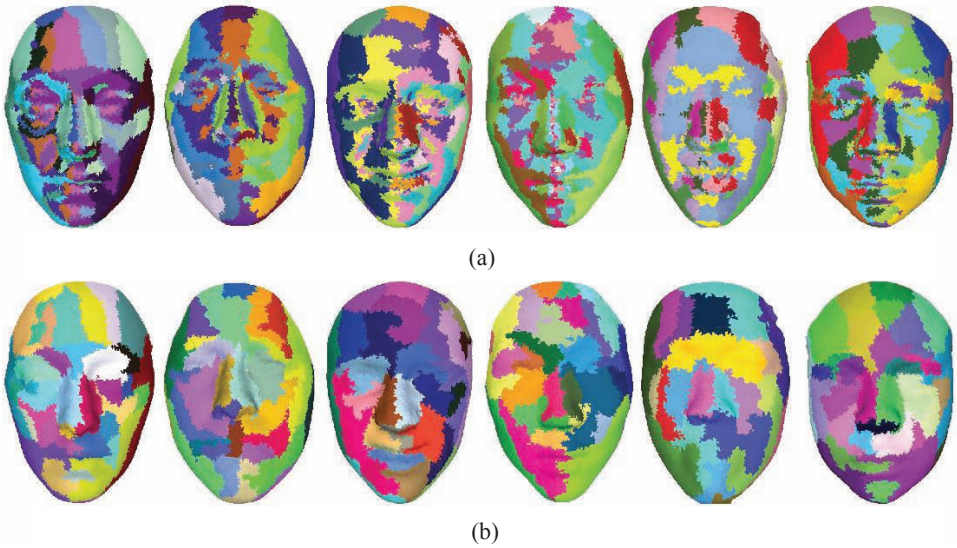

(a)

(b)

Fig. 2. Results of the face partitioning on the BU-3DFE database. (a) Results of k-means clustering, in which every color represents a cluster. (b) Results of the Graph-based Partitioning Algorithm, in which every color represents a patch.

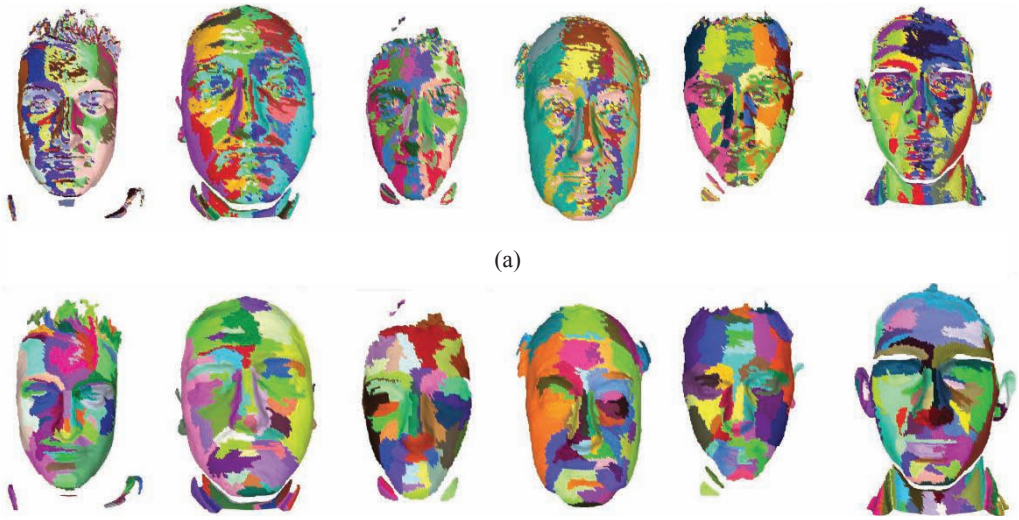

(a)

(b)

Fig. 3. Results of the face partitioning on the GavabDB database. (a) Results of the k-means clustering, in which every color represents a cluster. (b) Results of the Graph-based Partitioning Algorithm, in which every color represents a patch.

$$w(e_{ij}) = e^{-\frac{|n_i||n_j|}{n_i \cdot n_j}} = e^{-n_i \cdot n_j} \tag{4}$$

The edges that have zero weight are deleted and the remaining weights are sorted ascendingly into a list $W = \{w_1, w_2, w_3, \cdots, w_m\}$ according to the edge weight values.

As mentioned above, vertices from different parts of the 3D face can be included in the same cluster, which will cause difficulties in nose detection. To solve this problem, we separate the vertices within each cluster by accounting for the spatial connectivity. Every cluster is divided into a number of small patches, such that the vertices in each patch form a connected sub-graph of the original triangulation. Let the set of patches be $P = \{p_1, p_2, p_3, \cdots, p_n\}$. We define the size of a patch as the number of vertices in the patch. Patches that are too small are removed by iterative merging. A minimum patch size threshold λ is used to filter out the small patches. During the iterative process, every small patch that has a size below λ is merged with the nearest adjacent patch. Additionally the nearest adjacent patch is identified as the patch that is connected to the small patch by the edge that has the smallest weight. The merging process terminates when the size of each patch is larger than λ. Empirically, the vertices of the nose make up approximately 6% of the total vertices of the 3D face; hence, in practice, λ is set to $0.03N$ in our approach, where N is the total number of vertices in the 3D face. The final result is that the face is covered by a few large patches and each side of the nose corresponds to an individual patch. The graph-based partitioning algorithm is described in Algorithm 1.

Figs. 2.(b), 3.(b) and 4.(b) show the results of the

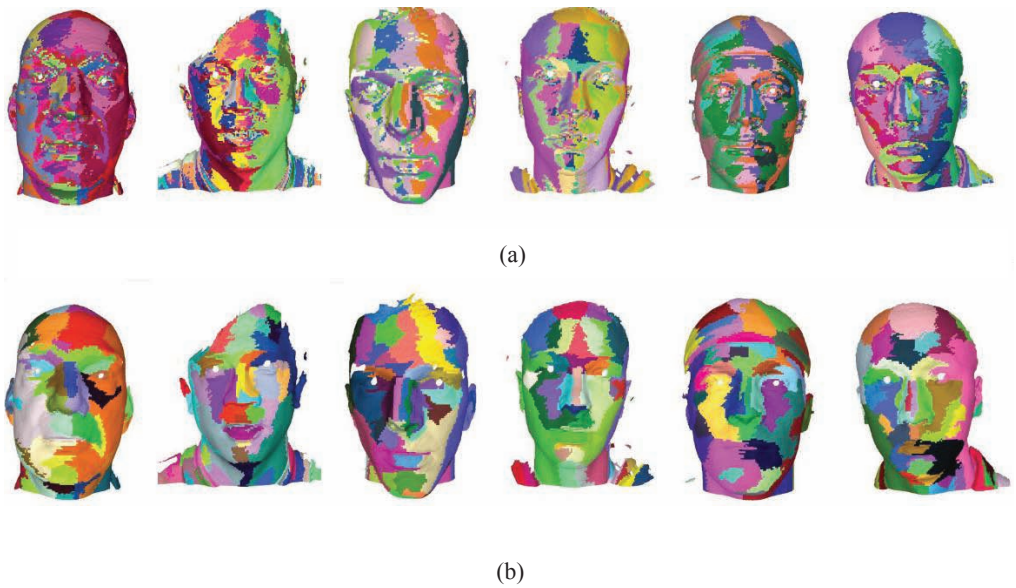

Fig. 4. Results of the face partitioning on the FRGC 2.0 database. (a) Results of k-means clustering, in which every color represents a cluster. (b) Results of the Graph-based Partitioning Algorithm, in which every color represents a patch.

Graph-based Partitioning Algorithm. In each figure, each color represents a patch, and as observed, the 3D faces are covered by a relatively small number of large patches, and the nose region is partitioned into two patches, one on each side of the nose. Using the partitioning result, we can easily detect the nose by selecting the two patches and combining them.

3) Feature Descriptor: To select the nose patches, we must find a descriptor that can differentiate the nose patches from other patches. Because of the distinctive shape of the nose, spin images [40] that are calculated at each inner vertex are utilized to describe a patch.

A spin image is a local shape descriptor that is initially introduced by Johnson and is used for surface matching. It is very similar to a space histogram and describes the relative distance between an oriented point and other points.

We use the mean of the spin images (MSI) to represent a patch. The MSI in a patch is defined as follows:

$$MSI_{P_r} = \frac{1}{|P_r|} \sum_{p_i \in P_r} S_{p_i} \tag{5}$$

where $|P_r|$ is the number of vertices in the patch P_r, and S_{p_i} is the spin image at vertex p_i. Because MSI accounts for all of the vertices in the patch, it offers an advantage for overcoming problems that are caused by noise, local deformation and resolution. In addition, MSI is robust to the pose variations because the spin images are object-centered representations. Fig. 5 shows examples of the MSIs of different patches. Fig. 5 (a) and (b) are spin images for the two sizes of the nose; (c) is for the left cheek; and (d) is for the right jaw.

4) Feature Detector: To detect the two nose patches, we must determine whether a patch is a part of the nose. This determination is a binary classification problem, and many methods have been proposed to address this issue. In our approach, we use a detector that is based on the popular SVM classifier [41]. The detector is generated by supervised training that utilizes the MSIs for different patches. We label the patches manually for training the SVM classifier.

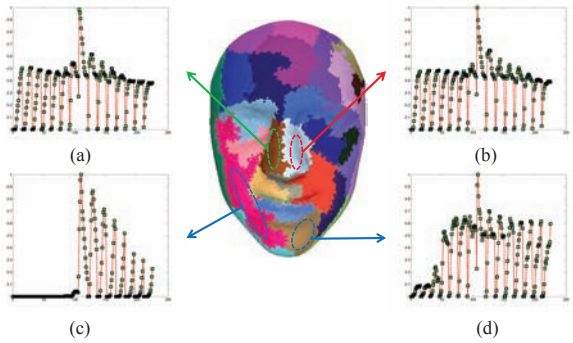

Fig. 5. *MSI* of different patches.

Our detector is applicable to a wide range of different 3D faces because the MSIs of the nose patches are similar for all of the 3D faces. Based on the output of the detector, only two patches are selected. The two selected patches are merged to obtain the nose region. Experimental results for the nose detection are given in Section IV.

B. Coarse Alignment

Once the location of the nose in the point cloud is known, alignment of the input face is possible. However, because our nose detection algorithm focuses on the whole nose region and the number of selected vertices for each input face is different, the 3D vertices in the nose region are unordered. It is difficult to obtain an accurate alignment using these vertices. In other words, only a coarse alignment is achieved for a 3D face alignment that is based on the nose.

As Fig. 6(b) shows, given an upright frontal 3D reference face, the test face and reference face can be related to each other by a 3D affine transformation [43].

$$v_r = t + R(\alpha_1, \alpha_2, \alpha_3) \cdot s \cdot v_t \quad (6)$$

where v_t and v_r denote the corresponding vertices on the test face and reference face; t denotes the translation vector; α_1, α_2, α_3 denote the three rotation parameters; R denotes the total rotation matrix; and s denotes the scale factor.

The rotation matrix is an orthogonal matrix that is the product of three individual rotation matrices:

$$R(\alpha_1, \alpha_2, \alpha_3) = R_1(\alpha_1) \cdot R_2(\alpha_2) \cdot R_3(\alpha_3)$$

where α_1, α_2 and α_3 are the rotation angles that are along the x, y and z axes, respectively. As described in [43], three control vectors are needed to obtain the rotation matrix in (6). In our approach, the rotation matrix is computed based on the detected nose. Given the two patches on either side of the nose, we first extract the average normals for each patch as follows

$$n_{P_r} = \frac{1}{|P_r|} \sum_{v_i \in P_r} n_i \quad (7)$$

where n_i is a unit normal vector at the vertex v_i and $|P_r|$ is the number of vertices in patch P_r.

Afterwards, we can obtain the third vector from the cross product of the two normal vectors. Given three mutually orthogonal vectors for the test face and reference face, the rotation matrix can be obtained.

The translation vector t can be obtained by computing the distance between the center of the bounding boxes for each nose. The scale factor s is estimated using the ratio of the sizes of the two bounding boxes.

Fig. 6 describes the work flow of our 3D face coarse alignment process.

C. Fine Alignment

Because only the nose vertices are involved in the coarse alignment, the normal vectors that are used to define the 3D affine coordinate transformation cannot exactly represent the orientation of the face. The coarse alignment is not sufficiently accurate to build the correspondences between the features of the test face and reference face. In our approach, an Iterative Closest Point (ICP) algorithm [2] is used to further refine the alignment. Because the expression of the test face is unknown, it is desirable to have a reference 3D face set $\mathcal{F}$ that consists of different expressions of a subject to perform the fine alignment.

The Iterative Closest Point (ICP) algorithm [2] has been proven to be valid for matching different 3D faces [45]. In our approach, the ICP algorithm is used to improve the alignment. The ICP algorithm is an iterative procedure for aligning two free-form shapes by minimizing the mean square error between the points in the test face f_t and the closest points in the reference face $f_r^m \in \mathcal{F}$. The algorithm terminates when the iteration exceeds a preset threshold. In our approach, the preset iteration number is set to 30 empirically. The algorithm outputs the affine transformation, including the rotation matrix R, translation vector t and scale parameter S. Only the face f_r^m that has the smallest error in $\mathcal{F}$ is chosen as the final reference face. After employing the ICP algorithm, the affine transformation parameters are applied to f_t to align it as closely as possible with the reference face f_r^m.

In the fine alignment, given a 3D face f_t that has an unknown expression, the ICP algorithm helps us to find the most suitable face f_r^m in the reference 3D face set F and align f_t to f_r^m in an iterative way.

Please note that $\mathcal{F}$ is only a fraction of the training database, which is composed of 25 expressive faces from one subject in the training database. In the training database, all of the 3D faces are pre-aligned well for the purpose of sharing the same number of vertices and the same topology.

III. Stage Two: Landmark Localization based on Local Coordinate Coding

The key aim of LCC-based landmark localization is to obtain the 3D coordinate of the landmarks of the input 3D face. In our approach, we first perform re-sampling to establish the dense vertex-wise correspondences between the input face and training database. Then, based on the 3D faces in the training database and their corresponding landmarks, we learn a coupled dictionary to model the relationship between the point cloud and the landmarks based on Local Coordinate Coding (LCC) [27]. Afterward, given the test 3D face, we can synthesize the 3D coordinate of the landmarks based on the learned coupled dictionary. Finally, the landmarks on the given test 3D face can be located under the guidance of the synthesized landmark coordinates.

A. Face Re-sampling

After alignment, the input 3D face is re-sampled by using the reference 3D face. The re-sampling involves the projection of each face onto a cylinder [30]. Fig. 7 illustrates the pipeline of the two-step re-sampling algorithm.

1) Cylindrical projection: After face alignment, the input face f_t and reference face f_r^m are projected onto a cylinder. For a vertex $p = [x_o, y_o, z_o]^T$, its cylindrical coordinates after projection are (u_o, v_o), where $u_o = \arccos(x_o/r)$, and $r = \sqrt{x_o^2 + z_o^2}$, $v_0 = y_0$.
2) Mesh image and re-sampling: To build the correspondence between the input face f_t and its reference face f_r^m, each vertex in f_t must be matched to a corresponding vertex in the reference face. To achieve this dense vertex-wise correspondence, we perform interpolation of the cylindrically projected f_t to obtain a high-resolution mesh image. Based on the cylindrical coordinates, the reference face can perform re-sampling on the mesh image. Finally, the re-sampled test 3D face is obtained, which has dense vertex-wise correspondence with the training face.

Because all of the training faces are well aligned in advance, the correspondence between the given test face and the reference face can also be applied to the other faces in the training database.

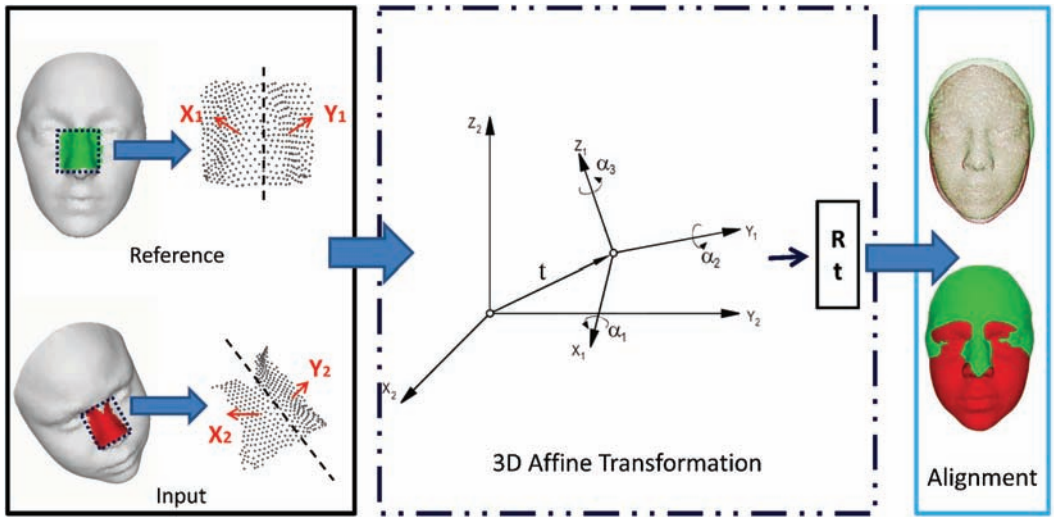

Fig. 6. Process of coarse alignment. (a) The reference face and input face. (b) 3D affine transformation. (c) Results of the coarse alignment.

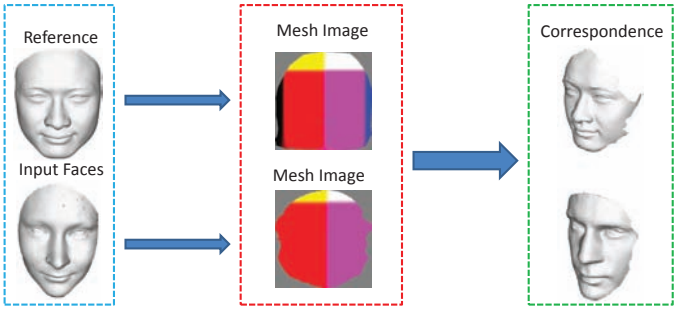

Fig. 7. Pipeline of 3D face re-sampling.

B. Coupled Dictionary Learning for Local Coordinate Coding

It is known that the landmarks occupy the important locations in the 3D face in such a way that they cover and describe the shape of the 3D face. In our coupled dictionary learning for local coordinate coding (LCC), we assume the 3D faces and their corresponding landmark sets from manifolds have similar local geometries in two different spaces [28], [29], [32]. Hence, we concatenate each training 3D face and its corresponding landmark set together as a sample. Given a sample $x = \{x_f, x_l\}$, we define x_f as the training 3D face, which contains N vertices, and x_l as its corresponding landmark set, which contains L vertices. Each vertex is defined with the 3D coordinate $v_i = (l_i^x, l_i^y, l_i^z)$. Thus, each input face is converted into a $3N \times 1$ vector, and the landmark set is a $3L \times 1$ vector for L landmarks. The LCC finds the best coding $\alpha(x) \in \mathbb{R}^M$ for x, which minimizes the reconstruction error and the violation of the locality constraint. This concept can be formulated as follows:

$$\min_{D \in \mathcal{C}, \alpha} \frac{1}{2}||x - D\alpha||^2 + \mu \sum_j |\alpha^j| \|d_j - x\|^2 \quad (8)$$

where $\mathcal{C} = \{D | \|d_i\| \leq 1, i = 1, \ldots, M\}$ is the convex feasible set of D. $D = [d_1, d_2, \cdots, d_M] \in \mathbb{R}^{3(N+L) \times M}$ is a set of bases or a dictionary. Here, $d_i = d_f(i), d_l(i)$, and $d_f(i)$, $d_l(i)$ are 3D face and landmark sets, respectively. It is important to constrain the columns of D because we can fix $D\alpha$ and the scale of D to make $\sum_j |\alpha^j| \|d_j - x\|^2$ arbitrarily small. The first term of the objective function measures the reconstruction error, and the second term preserves the locality of the coding.

Given a set of samples $\{x_1, x_2, \cdots, x_n\} \in \mathbb{R}^3(N+L)$, the bases or dictionary $D = [d_1 \cdots d_M] \in \mathbb{R}^{h \times M}$ can be learned by linearly approximating these samples as (8). For dictionary learning, we can minimize the summed objective function of all data samples over D and α simultaneously [33], [34], i.e.,

$$\min_{D \in \mathcal{C}, \alpha_i} \sum_i \left(\frac{1}{2}||x_i - D\alpha_i||^2 + \mu \sum_j |\alpha_i^j| \|d_j - x_i\|^2 \right) \quad (9)$$

where x_i is the i-th sample and α_i is its corresponding coding coefficient.

However, the above objective function is not jointly convex over D and α, which makes it difficult to solve. Nevertheless, it is convex over D with fixed α and vice versa. Therefore, we can optimize over D while keeping the value of α_i fixed, and then, we can optimize over α_i while keeping the value of D fixed. This alternating set of optimizations is performed until convergence.

For a fixed dictionary D and a sample x, optimizing over α can be transformed into optimizing the following equation over β:

$$\min_{\beta} \frac{1}{2}||x - D\Lambda^{-1}\beta||^2 + \mu \|\beta\|_1 \quad (10)$$

where Λ is a diagonal matrix whose diagonal elements are $\Lambda_{jj} = ||d_j - x||^2$ and $\beta = \Lambda\alpha$, and $||\beta||_1 = \sum_j |\beta^j|$ denotes the l_1-norm. In addition, we assume that $d_j \neq x$; thus, Λ^{-1} exists. After solving β, we can obtain $\alpha = \Lambda^{-1}\beta$. Here, α is an $m \times 1$ vector that has k non-zero elements, and $k \ll m$.

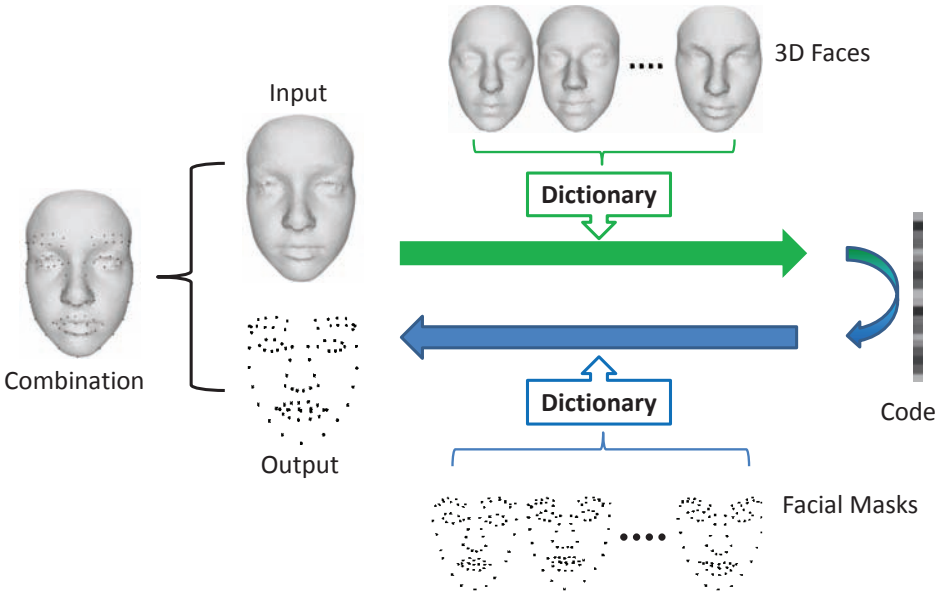

Fig. 8. Procedure for landmark localization.

For a fixed α, optimizing over D is a constrained quadratic programming problem. By expanding the squares in Eq. (9) and dropping the terms that do not have D, we can obtain

$$\begin{aligned} D=&\arg\min_{D\in\mathcal{C}} \sum_i \left(\frac{1}{2}||x_i - D\alpha_i||^2 + \mu \sum_j |\alpha_i^j| ||d_j - x_i||^2\right) \\ =&\arg\min_{D\in\mathcal{C}} \frac{1}{2} tr\Big[D^T D\Big(\sum_i \alpha_i {\alpha_i}^T + 2\mu\Sigma_i\Big)\Big] - tr\Big[D^T \cdot \\ &\Big(\sum_i x_i {\alpha_i}^T + 2\mu x_i \bar{\alpha}_i^T\Big)\Big] \end{aligned} \tag{11}$$

where $\bar{\alpha}_i$ is the component-wise absolute value of α_i, i.e., $\bar{\alpha}_i^j = |\alpha_i^j|$, and Σ_i is a diagonal matrix that is constructed from α_i.

Define two matrices, $A = \sum_i \alpha_i {\alpha_i}^T + 2\mu\Sigma_i$ and $B = \sum_i x_i {\alpha_i}^T + 2\mu x_i \bar{\alpha}_i^T$. Then, the optimal D can be found by performing a block-coordinate descent. In iteration k of the dictionary update, we update the j-th column d_j^k when the other columns are fixed. Denote a_j and $b-j$ as the j-th columns of the matrices A and B, a_{jj} as the (j,j)-th element of A, and the dictionary D^k at iteration k. The updating rule is as follows

$$d_j^{k+1} = \Pi\left(d_j^k - \frac{1}{a_{jj}}\left(D^k a_j - b_j\right)\right) \tag{12}$$

where $\Pi(\cdot)$ is the projection operator onto the feasible set of D.

The detail of the coupled dictionary learning algorithm is given in Algorithm 2.

Algorithm 2 Coupled Dictionary Learning

Input: Training database $\{x_1, x_2, \cdots, x_n\}$,
Initial dictionary D_0, μ.
Output: Learned dictionary D_n
Initialize: $A_0 \leftarrow 0$, $B_0 \leftarrow 0$
1. **for** $t \leftarrow 1$ to n **do**
2. Draw a sample x_t from the training database.
3. Local coordinate coding: compute using Eq. (10)
$\alpha_t = \arg\min_\alpha \frac{1}{2}\|x_t - D_{t-1}\alpha\|^2 + \mu \sum_j |\alpha^j| \| \left(D_{t-1}\right)_j - x_t\|^2$
4. Update $A_t \leftarrow A_{t-1} + \alpha_t \alpha_t^T + 2\mu\Sigma_t$.
5. Update $B_t \leftarrow B_{t-1} + x_t \alpha_t^T + 2\mu x_t \bar{\alpha}_t^T$.
7. Update dictionary using Eq. (12)
$d_j^t = \Pi\left(d_j^{t-1} - \frac{1}{a_{jj}}\left(D^{t-1}a_j - b_j\right)\right)$.
8. **end for**
9. **return** D_n

C. Landmark Localization

In contrast to the previous feature detection-based method and the statistical PDM-based method, in our approach, we synthesize the landmarks first instead of detecting or fitting them through some local feature descriptor or statistical point distribution model. This concept enables us to perform the landmark localization robustly over the whole face and to adapt to changes in the extent to which the 3D data cover the face.

As Fig. 8 shows, some sample faces and their corresponding landmarks are selected as the training data to learn the two dictionaries for the LCC.

Given that the coupled dictionary is learned, let x_f be an input 3D face, let D_f be the 3D face dictionary, and let α be the coefficients of D_f. The approximation to x_f can then be formulated as follows:

$$x_f^{'} = \sum D_f \alpha \tag{13}$$

It is obvious that the LCC solution has only a few significant values in α because of the locality constraint that we demonstrated in Eq. (8). Hence, the above process can be transformed into the problem of selecting the local bases for a given 3D face x_f to form a local coordinate system.

$$\begin{aligned} &\min_c \textstyle\sum_x \|x_f - D_f\alpha\|^2 \\ \text{s.t.} \quad &1^T\alpha = 1 \end{aligned} \tag{14}$$

As discussed in Section III-B, we assume that the 3D faces and their corresponding landmark sets form manifolds that have similar local geometries in two different spaces [32]. Hence, we can approximate the corresponding landmark set x_l by using the same coefficients for $x_f^{'}$. By replacing the 3D face dictionary D_f with the landmark dictionary D_l, we can obtain the corresponding synthesized landmark set $x_l^{'}$:

$$x_l^{'} = \sum D_l\alpha \tag{15}$$

Considering that $x_l^{'}$ is synthesized based on dictionary D_l, it is clear that $x_l^{'}$ is not exactly equal to the landmark set x_l, even though it is very close to it. It is desirable to employ vertices that are in the 3D face instead of synthesized vertices to be the landmarks. Thus, in our approach, we further find the vertices that are closest to the synthesized landmarks to be our localization result. Given $x_l^{'} = \{v_i^{'}\}_{1\leq i\leq L}$ and $x_l = \{v_i\}_{1\leq i\leq L}$,

$$v_i = \min_{v_j} \|v_i^{'} - v_j\|^2 \tag{16}$$

where $v_j \in x_f$

Finally through the above steps, each input 3D face is marked with the corresponding landmarks.

IV. Experimental Results

A. Database

In this section, we test our method on the BU-3DFE database [35], GavabDB database [36] and FRGC 2.0 database [37]. The experimental results are demonstrated in the following subsections.

The BU-3DFE database contains 100 subjects (56% female, 44% male), who range in age from 18 to 70 years and who have a variety of ethnic/racial ancestries. There are 25 instant 3D expression models for each subject, which results in a total of 2,500 3D facial expression models. In addition, the BU-3DFE database provides 83 landmarks for each 3D face, which help us to train and test our proposed landmark localization method.

The GavabDB database contains 549 3D images of facial surfaces. The meshes in the database correspond to 61 different individuals with different poses and facial expressions.

The FRGC 2.0 database is sponsored by several government agencies and contains hundreds of frontal 2D face images and 3D face meshes. Different poses and expressions are observed in the 3D faces.

Note that because the proposed method is based on nose detection, we chose only the 3D faces that have noses in our experiments.

B. Nose Detection

Before conducting the experiments, 50 faces from various ancestries and with various expressions are selected for training an SVM model. Because the MSI of the nose patches differs greatly from those of other patches, as Fig. 5 shows, a simple linear kernel is used in the SVM classifier. After detection, the detected noses are shown in red on the frontal faces for better display.

For the nose detection on the BU-3DFE database, the testing faces can be divided into two sets. Set 1 consists of faces that have only yaw rotations, slight expression variations and missing data. Set 2 consists of faces that have combinations of yaw rotation, pitch rotation, roll rotation, and extreme expression variations. Because the 3D faces in the BU-3DFE database are frontal, we rotate these models for evaluation.

Some representative experimental results that are obtained from Set 1 and Set 2 are shown in Fig. 9. Figs. 9 (a) and (b) illustrate the nose detection results for Set 1. As the figure shows, our approach correctly detects the noses of 3D faces that have different yaw rotations and expressions, even when there is a hole that is caused by missing data. Figs. 9 (c) and (d) illustrate the nose detection results for Set 2. Faces from Set 2 have combinations of yaw rotation, pitch rotation and roll rotation along with extreme expression variations. As the figure shows, our approach still correctly detects the noses of the 3D faces.

To validate the proposed nose detection method, we experiment further with the GavabDB and FRGC 2.0 databases. These two databases consist of many originally non-frontal faces. Collars, necks and missing data are challenges for our proposed nose detection method. Some representative experimental results are shown in Figs. 10 and 11.

C. Face Alignment

Nair *et al.* [4] also presented an ICP-based 3D face alignment approach, in which the curvature information is utilized to find the facial features to make a coarse alignment before performing the ICP-based fine alignment. To evaluate the performance of our approach, we make a comparison between the Nair *et al.* approach and our approach.

The alignment is successful when the average pixel-wise error between the test face and reference face is less than 2 mm. The alignment rate is the ratio between the number of successfully aligned faces and the total number of tested faces. All of the methods have been programmed using Matlab 7.11 on a PC with an Intel(R) Core(TM)2 Duo CPU E5800 3.16 GHz and 4 GB RAM. Here, 1500 3D faces from different databases are used for testing.

In the evaluation, 1500 faces are randomly selected from the three databases for testing. Both neutral and expressive 3D faces are included. Each 3D face is rotated around the x-axis, y-axis and z-axis. The angle of rotation around each axis is generated randomly and ranges from $-\pi$ to π. We divide the testing faces into three groups according to their expressions: neutral, mild and extreme.

We give the average accuracy in Table I. The alignment error measures the average distance in millimeters between

Fig. 9. (a) Examples of 3D faces in Set 1. (b) The nose detection results of Set 1. (c) Examples of 3D faces in Set 2. (d) The nose detection results of Set 2. Note that the nose detection results are shown by rotating the input faces into frontal views.

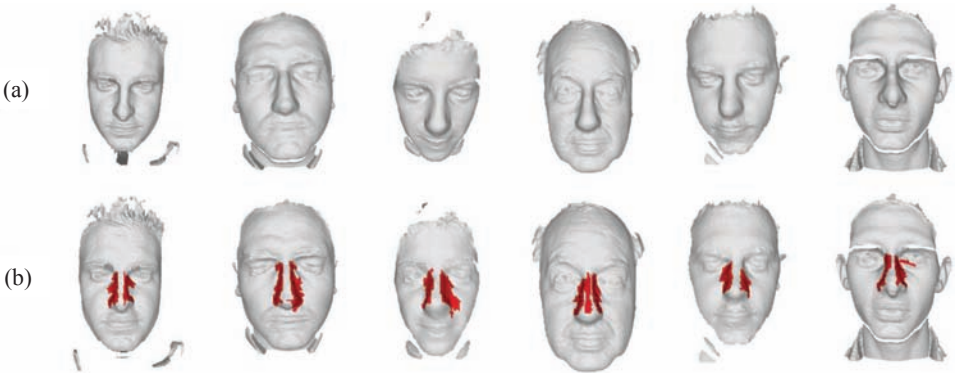

Fig. 10. (a) Examples of input 3D faces. (b) The nose detection results of the GavabDB database.

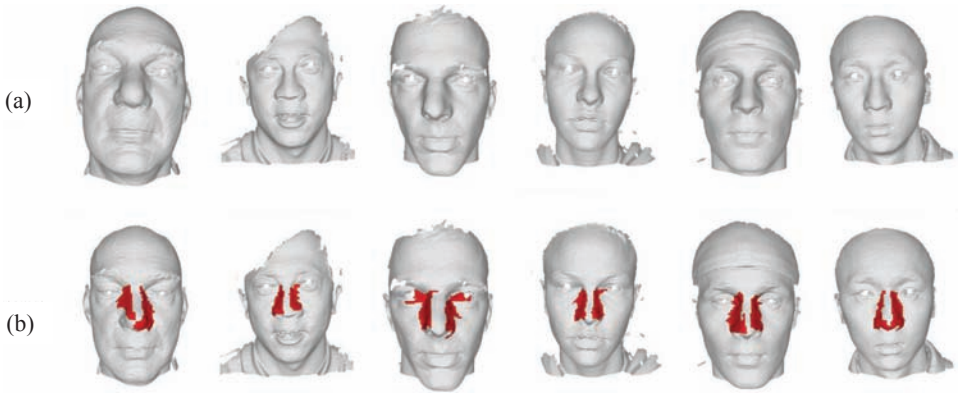

Fig. 11. (a) Examples of input 3D faces. (b) The nose detection results of the FRGC database.

TABLE I
PERFORMANCE OF NOSE DETECTION BASED 3D FACE ALIGNMENT

Expression	Neutral			Mild			Extreme		
Samples	512			603			385		
Error (mm)	mean	std.	$<$ 2 mm	mean	std.	$<$2 mm	mean	std.	$<$2 mm
Nair *et al.* [4]	2.07	1.74	77.4%	3.13	2.54	67.3%	5.15	3.75	50.9%
Ours	1.45	1.27	94.5%	1.97	1.51	93.7%	2.45	1.93	80.8%

TABLE II
ACCURACY COMPARISON ON THE ROTATED NEUTRAL 3D FACES (OC FOR OUTER CONTOUR, OUL FOR OUTER UPPER LIP, OLL FOR OUTER LOWER LIP, ILL FOR INNER LOWER LIP, IUL FOR INNER UPPER LIP, LE FOR LEFT EYE, RE FOR RIGHT EYE, NE FOR NOSE, LEB FOR LEFT EYE-BROW, REB FOR RIGHT EYE-BROW.)

Method	RF-AAM [16]			PDM [4]			SS-PDM [10]			Ours		
Error	$<$5 mm	mean	std.	$<$ 5 mm	mean	std.	$<$5 mm	mean	std.	$<$5 mm	mean	std.
OC	84.5%	3.38	3.35	33.0%	8.95	7.85	72.1%	4.21	2.36	91.2%	2.91	2.01
OUL	83.4%	3.50	2.51	35.0%	8.47	7.12	63.5%	5.12	3.32	88.7%	3.05	2.23
OLL	85.8%	3.22	2.31	26.1%	11.73	10.11	62.8%	5.21	3.23	85.3%	3.31	2.21
ILL	87.6%	3.12	2.15	25.6%	12.26	11.12	62.0%	5.32	3.31	89.2%	2.89	2.16
IUL	87.1%	3.14	2.13	29.4%	10.57	10.14	66.0%	4.75	3.01	88.9%	2.91	2.15
LE	86.6%	3.17	2.57	37.3%	7.75	6.75	74.5%	4.05	2.24	93.1%	2.59	2.31
RE	87.4%	3.13	2.55	37.8%	7.28	6.73	73.3%	4.12	2.57	93.0%	2.61	2.33
NE	78.8%	3.77	2.79	79.7%	3.75	2.23	88.4%	3.09	2.21	93.4%	2.55	2.22
LEB	77.6%	3.87	2.80	26.6%	11.63	10.73	66.5%	4.73	2.41	88.3%	2.99	2.84
REB	77.7%	3.86	2.83	26.6%	11.62	22.23	67.4%	4.53	2.34	89.2%	3.03	2.82

TABLE III
ACCURACY COMPARISON ON THE ROTATED MILD EXPRESSIVE 3D FACES.

Method	RF-AAM [16]			PDM [4]			SS-PDM [10]			Ours		
Error	$<$5 mm	mean	std.	$<$ 5 mm	mean	std.	$<$5 mm	mean	std.	$<$5 mm	mean	std.
OC	59.6%	5.48	4.43	20.6%	16.65	12.75	63.5%	5.11	4.76	71.5%	4.27	3.23
OUL	83.2%	3.51	3.33	26.0%	12.21	13.43	53.6%	5.82	4.32	88.7%	3.07	2.73
OLL	53.7%	5.78	4.50	21.4%	15.73	15.11	34.6%	7.21	5.23	81.2%	3.63	3.32
ILL	58.0%	5.52	4.73	21.9%	15.62	15.31	34.6%	7.22	5.31	71.3%	4.27	3.42
IUL	54.3%	5.74	4.73	28.0%	11.37	9.41	45.7%	6.15	5.01	86.6%	3.17	2.75
LE	82.7%	3.56	3.27	29.4%	10.57	9.46	63.2%	5.15	5.01	86.6%	3.17	2.75
RE	83.7%	3.47	3.15	29.9%	10.28	9.13	63.5%	5.12	2.57	92.3%	2.74	2.45
NE	65.0%	4.86	3.47	33.6%	8.75	7.23	69.4%	4.39	3.21	93.3%	2.56	2.41
LEB	62.3%	5.27	4.71	20.4%	16.73	13.23	45.0%	6.23	5.41	88.4%	3.10	2.98
REB	62.3%	5.26	4.73	20.8%	16.32	12.43	46.8%	6.08	2.34	88.9%	3.05	2.82

TABLE IV
ACCURACY COMPARISON ON THE ROTATED EXTREME EXPRESSIVE 3D FACES.

Method	RF-AAM [16]			PDM [4]			SS-PDM [10]			Ours		
Error	$<$5 mm	mean	std.	$<$ 5 mm	mean	std.	$<$5 mm	mean	std.	$<$5 mm	mean	std.
OC	47.8%	6.01	5.65	15.4%	20.73	17.75	47.2%	6.04	5.43	67.2%	4.55	4.02
OUL	82.2%	3.52	3.01	24.0%	13.78	13.43	43.7%	6.43	5.67	88.4%	3.10	3.27
OLL	39.1%	6.63	5.31	17.9%	18.33	17.11	35.5%	7.95	6.99	76.7%	3.90	3.83
ILL	45.6%	6.22	5.42	20.0%	17.64	16.23	35.8%	8.20	7.41	67.8%	4.51	3.66
IUL	35.3%	7.14	5.87	27.0%	11.57	10.22	38.8%	6.67	5.31	85.3%	3.25	2.99
LE	77.6%	3.68	2.99	25.1%	12.75	11.65	47.5%	6.01	4.74	92.2%	2.77	2.71
RE	80.0%	3.70	3.62	24.7%	12.98	11.31	46.7%	6.09	4.81	91.7%	2.81	2.83
NE	55.5%	5.68	4.85	24.2%	13.75	12.11	65.4%	4.80	4.11	93.3%	2.57	2.43
LEB	59.7%	5.47	5.16	19.7%	17.93	16.25	41.2%	6.54	4.81	86.4%	3.18	3.05
REB	52.9%	5.82	5.19	19.0%	18.04	17.03	45.9%	6.13	4.33	88.6%	3.07	2.93

the corresponding vertices in the test face and reference face. Table I shows that our method outperforms Nair *et al.* method in all of the expression groups. Nair *et al.* method uses three thresholds to identify the salient high-curvature regions, concave regions and convex regions, which are not robust if there are large deformations in the 3D faces. In contrast, our approach is more robust to the variations in the expressions because the 3D shape of the nose is stable. Additionally, with regard to the run time, Nair *et al.* method takes 44.178 seconds to process one 3D face, while our method takes 9.71 seconds.

D. Landmark Localization

Comprehensive and quantitative evaluations have been performed in our experiments. Comparisons between RF-AAM [16], Nair *et al.* work (PDM for short) [4], Perakis *et al.* work (SS-PDM for short) [10] and our approach are performed on the tolerance to different rotations, expressions and resolutions. To compare the accuracy of the landmark locations comprehensively, we divide the 83 landmarks into several groups: 15 for the outer contour (chin and cheeks), seven for the outer upper lip (outer mouth corners and upper outer lip), five for the outer lower lip, three for the inner lower lip, five for the inner upper lip (inner mouth corners and inner upper lip), eight for the left eye, eight for the right eye, 12 for the nose, 10 for the left eye brow and 10 for the right eye brow. The Euclidean distance in millimeters between the located landmark and the ground truth is used to measure the error.

TABLE V
ACCURACY COMPARISON ON THE BU-3DFE DATABASE FACES. EACH FACE CONTAINS APPROXIMATELY 35K VERTICES.

Method	RF-AAM [16]			PDM [4]			SS-PDM [10]			Ours		
Error	<5 mm	mean	std.	< 5 mm	mean	std.	<5 mm	mean	std.	<5 mm	mean	std.
OC	64.8%	4.89	4.35	22.3%	15.45	13.75	63.5%	5.12	4.73	76.5%	3.91	3.02
OUL	83.2%	3.51	2.53	27.3%	11.47	10.12	53.6%	5.79	4.17	88.7%	3.07	2.57
OLL	62.8%	5.22	5.31	22.5%	15.23	10.11	38.0%	6.79	5.23	81.7%	3.61	3.23
ILL	64.6%	4.92	4.45	22.7%	15.16	10.22	37.3%	6.91	5.41	76.9%	3.89	3.66
IUL	61.8%	5.34	5.33	28.3%	11.17	9.34	52.5%	5.85	4.31	87.7%	3.11	2.75
LE	83.7%	3.47	2.57	29.8%	10.34	8.85	63.8%	5.07	2.74	92.5%	2.69	2.41
RE	84.0%	3.43	2.55	30.3%	10.18	8.63	63.5%	5.11	3.47	92.4%	2.72	2.43
NE	65.7%	4.77	3.79	34.1%	8.67	7.21	73.7%	4.09	2.41	93.3%	2.56	2.23
LEB	65.0%	4.87	3.81	22.3%	15.43	13.34	52.7%	5.83	3.42	88.4%	3.09	2.95
REB	64.0%	4.98	3.87	22.3%	15.32	12.23	56.8%	5.58	3.33	88.9%	3.05	2.93

TABLE VI
ACCURACY COMPARISON ON THE SUBSAMPLED BU-3DFE DATABASE FACES. EACH FACE CONTAINS APPROXIMATELY 8.7K VERTICES.

Method	RF-AAM [16]			PDM [4]			SS-PDM [10]			Ours		
Error	<5 mm	mean	std.	< 5 mm	mean	std.	<5 mm	mean	std.	<5 mm	mean	std.
OC	58.3%	5.43	4.83	17.2%	18.54	20.62	42.3%	7.68	7.10	76.3%	3.94	3.05
OUL	74.9%	3.90	2.81	21.0%	13.76	15.18	35.7%	8.69	6.26	88.4%	3.10	2.60
OLL	56.5%	5.79	5.89	17.3%	18.28	15.17	25.3%	10.19	7.85	81.2%	3.64	3.25
ILL	58.1%	5.46	4.94	17.5%	18.19	15.33	24.9%	10.37	8.12	76.5%	3.92	3.22
IUL	55.6%	5.93	5.92	21.8%	13.4	14.01	35.0%	8.78	6.47	87.1%	3.14	2.74
LE	75.3%	3.85	2.85	22.9%	12.41	13.28	42.5%	7.61	4.11	92.5%	2.70	2.43
RE	75.6%	3.81	2.83	23.3%	12.22	12.95	42.3%	7.67	5.21	92.4%	2.71	2.41
NE	59.1%	5.29	4.21	26.2%	10.40	10.82	49.1%	6.14	3.62	93.2%	2.57	2.32
LEB	58.5%	5.41	4.23	17.2%	18.52	20.01	35.1%	8.75	5.13	87.6%	3.12	2.91
REB	57.6%	5.53	4.30	17.2%	18.38	18.35	37.9%	8.37	5.00	87.7%	3.10	2.95

TABLE VII
ACCURACY COMPARISON OF THE INTERPOLATED BU-3DFE DATABASE FACES. EACH FACE CONTAINS APPROXIMATELY 140K VERTICES.

Method	RF-AAM [16]			PDM [4]			SS-PDM [10]			Ours		
Error	<5 mm	mean	std.	< 5 mm	mean	std.	<5 mm	mean	std.	<5 mm	mean	std.
OC	43.7%	7.26	7.45	22.4%	15.43	13.75	63.5%	5.10	4.53	76.4%	3.92	3.00
OUL	56.1%	5.21	2.78	27.0%	11.42	10.12	54.3%	5.72	4.10	88.5%	3.09	2.55
OLL	42.3%	7.75	5.84	22.7%	15.10	10.11	38.2%	6.75	5.14	81.7%	3.60	3.25
ILL	43.5%	7.30	5.79	22.7%	15.11	10.22	37.4%	6.87	5.25	77.7%	3.86	3.64
IUL	41.7%	7.92	6.40	28.3%	11.20	9.34	52.5%	5.85	4.22	87.7%	3.10	2.77
LE	54.2%	5.15	3.61	29.8%	10.31	8.85	64.0%	4.97	2.66	92.7%	2.67	2.45
RE	54.3%	5.09	3.65	30.6%	10.13	8.63	64.0%	5.00	3.40	92.4%	2.71	2.44
NE	42.5%	7.08	4.73	34.5%	8.54	7.21	76.9%	3.89	2.35	93.3%	2.57	2.21
LEB	42.1%	7.23	4.67	22.1%	15.36	13.34	55.5%	5.70	3.40	87.6%	3.11	2.90
REB	41.4%	7.39	4.78	22.2%	15.34	12.23	58.0%	5.54	3.28	88.9%	3.04	2.91

We use the BU-3DFE database to make the quantitative evaluation because it contains 100 subjects while posing six different expressions that have varying levels of intensity. Each 3D face contains approximately 35K vertices. More importantly, each 3D face in the BU-3DFE database is annotated with the location of 83 landmarks, which can be used as the ground truth for the quantitative evaluation. A total of 1250 3D faces and their corresponding landmarks from 50 subjects in the BU-3DFE database are used as training data and the others for testing. For our LCC-based landmark localization, all of the training faces are preprocessed to have vertex-wise correspondence. And the average interpupillary distance (IPD) of the test faces is 68.9 mm. For the other existing methods, the training settings are the same as those in [16], [4] and [10]. In addition, we train a random forest [15] for the initialization of RF-AAM, as discussed in [16]. Apart from RF-AAM, the other landmarking methods, Nair *et al.* and Perakis *et al.* are trained according to [4] and [10], respectively.

To compare the tolerance to rotations and expressions, each 3D face of the testing data is rotated around the x-axis, y-axis and z-axis. The angle of rotation around each axis is generated randomly and ranges from $-\pi$ to π. Additionally, the testing data are divided into three groups in terms of their expression intensity: neutral, mild and extreme. The performance of RF-AMM, PDM, SS-PDM and our approach are given in Tables II, III and IV. The experimental results show that our approach outperforms the state of these art methods by providing more stable and accurate locations when there are different poses for the 3D face.

In addition to the above evaluation, we test the tolerance to different resolutions. In addition to using the rotation operation mentioned above, each 3D face is subsampled twice and interpolated in a bilinear way. Note that all of the localizers are trained only with the data that does not have any resolution changes to evaluate their tolerance to variations in the resolution. Table V shows the average accuracy on the rotated testing data without resolution changes, in which each 3D face contains approximately 35K vertices. Table VI shows the average accuracy on the subsampled data in which each 3D face contains approximately 8.7K vertices. Additionally Table VII shows the average accuracy on the interpolated data in which each 3D face contains approximately 140K vertices. The experimental results show that our method achieves high accurate landmark localization which is robust to variations

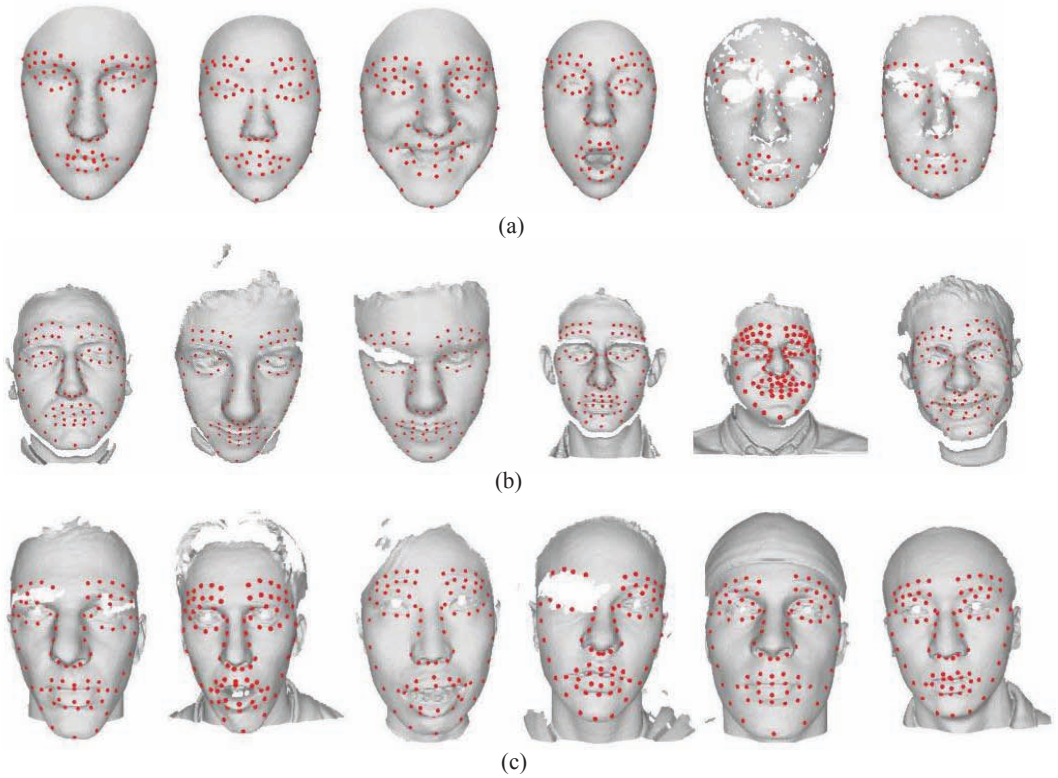

Fig. 12. Examples of our landmark localizing results on the (a) BU-3DFE, (b) GavabDB and (c) FRGC 2.0. databases

in pose, expression, resolution and face incompleteness. PDM and SS-PDM produce similar results on high-resolution data but are worse on low-resolution data. RF-AAM is sensitive to the variations in the resolution because both the template patch for the AAM training and the patch for the random forest-based posed estimation are fixed in size.

Examples of our landmark localizing results on the BU-3DFE database are given in Fig. 12(a). We also perform our landmark localization on the Gavab and FRGC 2.0 databases. The examples of the results are shown in Figs. 12(b) and (c). Some of the examples show that our approach can produce the landmarks robustly even in cases in which the 3D faces are not completely covered by the data.

V. Conclusions and Future Work

In this paper, we present a local coordinate coding-based approach to automatically locate the landmarks of a 3D face robustly and accurately. The proposed approach consists of two stages: nose detection-based 3D face alignment and LCC-based landmark localization. In the first stage, nose detection is accomplished by partitioning the 3D face into several patches and then selecting the nose patches using an SVM classifier. Once the nose is detected, a coarse alignment is obtained between the test face and reference face. This alignment is followed by an ICP-based fine alignment. In the second stage, we re-sample on a given 3D face to build a vertex-wise correspondence with the reference face and to obtain a training dictionary of the LCC-based landmark localization. Then, an LCC-based coupled dictionary learning algorithm for landmark localization is presented. Finally, the landmark coordinates are obtained by finding the vertices that are closest to the synthesized landmarks based on the LCC.

The experimental results show that our method achieves high accurate landmark localization which is robust to variations in the pose, expression, resolution and face incompleteness. In the future, we will expand our work to the area of 3D face recognition and facial expression synthesis based on alignments.

References

[1] X. Lu, and A.K. Jain, "Automatic feature extraction for multiview 3D face recognition," *Proc. 7th Conf. Automatic Face and Gesture Recognition*, 2006, pp. 585-590.

[2] P.J. Besl, and N.D. McKay, "A method for registration of 3-D shapes," *IEEE Trans. Pattern Anal. Mach. Intell.*, volume 14, 1992, pp. 239-256.

[3] P. Perakis, T. Theoharis, G. Passalis, and I.A. Kakadiaris, "Automatic 3D facial region retrieval from multi-pose facial datasets," *Proc. Eurographics Workshop on 3D Object Retrieval*, 2009, pp. 37-44.

[4] P. Nair, and A. Cavallaro, "3-D Face detection, landmark localization, and registration using a point distribution model," *IEEE Trans. Multimedia*, volume 1, 2009, pp. 611-623.

[5] D. Colbry, G. Stockman, and A. Jain, "Detection of anchor points for 3D face verification," *IEEE Workshop on Advanced 3D Imaging for Safety and Security*, 2005, pp. 118.

[6] T.H. Lin, W.P. Shih, W.C. Chen, and W.Y. Ho, "3D face authentication by mutual coupled 3D and 2D feature extraction," *Proc. 44th ACM Southeast Conference*, 2006, pp. 423-427.

[7] M.P. Segundo, C. Queirolo, O.R.P. Bellon, and L. Silva, "Automatic 3D facial segmentation and landmark detection," *Proc. 14th Int. Conf. Image Analysis and Processing*, 2007, pp. 431-436.

[8] C. Dorai, and A.K. Jain, "COSMOS - A representation scheme for 3D free-form objects," *IEEE Trans. Pattern Anal. Mach. Intell.*, volume 19, 1997, pp. 1115-1130.

[9] A.S. Mian, M. Bennamoun, and R. Owens, "An efficient multimodal 2D-3D hybrid approach to automatic face recognition," *IEEE Trans. Pattern Anal. Mach. Intell.*, volume 29, 1007, pp. 1927-1943.

[10] P. Perakis, G. Passalis, T. Theoharis, and I. A. Kakadiaris, "3D Facial Landmark Detection under Large Yaw and Expression Variations," *IEEE Trans. Pattern Anaysis and Machine Intelligence*, 2012.

[11] H. Dibeklioğlu, A.A. Salah, and L. Akarun, "3D Facial landmarking under expression, pose, and occlusion variations," *Proc. Int. Conf. Biometrics: Theory, Applications and Systems*, 2008, pp. 1-6.

[12] M. Romero-Huertas, and N. Pears, "3D Facial Landmark Localisation by Matching Simple Descriptors," *Proc. Int. Conf. Biometrics: Theory, Applications and Systems*, 2008, pp. 1-6.

[13] T.F. Cootes, C.J. Taylor, D.H. Cooper, and J. Graham, "Active shape models-their training and application," *Computer Vision and Image Understanding*, volume 61, No. 1, 1995, pp. 38-59.

[14] C. Creusot, N. Pears, J. Austin, "A machine-learning approach to keypoint detection and landmarking on 3D meshes," *International Jounal of Computer Vision*, 102:147-179, 2013.

[15] G. Fanelli, M. Dantone, J. Gall, A. Fossati, and L. Van Gool, "Random forests for real time time 3D face analysis," *International Journal of Computer Vision*, 101: 437–458, 2013.

[16] G. Fanelli, M. Dantone, and L. Van Gool, "Real time 3D face alignment with random forests-based active appearance models," *IEEE Conference on Automatic Face and Gesture Recognition*, pp. 1-8, 2013.

[17] G. J. Edwards, C. J. Taylor, and T. F. Cootes. "Interpreting face images using active appearance models," *Proc. Int. Conf. Automatic Face and Gesture Recognition*, June 1998, pp. 300-305.

[18] T. Cootes, G. Edwards, and C. Taylor. "Active appearance models," *Proc. European Conf. Computer Vision*, volume 2, 1998, pp. 484-498.

[19] T. Cootes, G. Edwards, and C. Taylor. "A comparative evaluation of active appearance models algorithms," *Proc. British Machine Vision Conference*, 1998, pp. 680-689.

[20] T. F. Cootes. "Statistical models of appearance for computer vision," Online technical report available from http://www.isbe.man.ac.uk/ bim/refs.html, Sept. 2001.

[21] T. F. Cootes, G. J. Edwards, and C. J. Taylor. "Active appearance models," *IEEE Trans. Pattern Anal. Mach. Intell.*, volume 23, 2001, pp. 681-685.

[22] T. Cootes and P. Kittipanya-ngam. "Comparing variations on the active appearance model algorithm," *In Proceedings of the British Machine Vision Conference*, volume 2, 2002, pp. 837-846.

[23] A. Batur and M. Hayes, "Adaptive active appearance models," *IEEE Transactions on Image Processing.*, vol. 14, no. 11, 2005, pp. 1707-1721.

[24] J. Zhu, S.C.H. Hoi, E. Yau, and M.R. Lyu, "Automatic 3D face modeling using 2D active appearance models," *Proceedings of the 13th Pacific Conference Computer Graphics and Applications*, 2005, pp. 133-135.

[25] K.S. Cho, Y.G. Kim, and G.S. Shin, "Fast 3D face synthesis using AAM, Advanced Intelligent Computing Theories and Applications," *With Aspects of Contemporary Intelligent Computing Techniques*, 2007, pp. 1119-1125.

[26] C.W. Chen, and C.C. Wang, "3D active appearance model for aligning faces in 2D images," *Proceedings of the IEEE/RSJ Int. Conf. Intelligent Robots and Systems*, 2008, pp. 3133-3139.

[27] K. Yu, T. Zhang, and Y. Gong, "Nonlinear learning using local coordinate coding," *Advances in Neural Information Processing Systems*, volume 22, 2009, pp. 2223-2231.

[28] L. Shao, R. Yan, X. Li and Y. Liu, "From heuristic optimization to dictionary learning: a review and comprehensive comparison of image denoising algorithms," *IEEE Transactions on Cybernetics*, vol. 44, no. 7, pp. 1001-1013, 2014.

[29] L. Zhang, X. Zhen and L. Shao, "Learning object-to-class kernels for scene classification," *IEEE Transactions on Image Processing*, vol. 23, no. 8, pp. 3241-3253, 2014.

[30] M. Song, Z. Dong, C. Theobalt, H. Wang, Z. Liu, and H.P. Seidel, "A generic framework for efficient 2-D and 3-D facial expression analogy," *IEEE Trans. on Multimedia*, volume 9, no. 7, 2007, pp. 1384-1395.

[31] M. Song, C. Chen, J. Bu, T. Sha, "Image-based facial sketch-to-photo synthesis via online coupled dictionary learning," *Information Sciences*, vol. 193, 2012, pp. 233-246.

[32] D. Tao, X. Li, X. Wu, S. J. Maybank, "Geometric mean for subspace selection," *IEEE Trans. Pattern Analysis and Machine Intelligence*, 2009, pp. 260-274.

[33] R. Yan, L. Shao and Y. Liu, "Nonlocal hierachical dictionary learning using wavelets for image denoising," *IEEE Transactions on Image Processing*, vol. 22, no. 12, pp. 4689-4698, 2013.

[34] F. Zhu and L. Shao, "Weakly-supervised cross-domain dictiornary learning for visual recognition," *International Journal of Computer Vision*, vol. 109, no. 1-2, pp. 42-59, 2014.

[35] L. Yin, X. Wei, Y. Sun, J. Wang, and M.J. Rosato, "A 3D facial expression database for facial behavior research," *Proc. 7th Int. Conf. Automatic Face and Gesture Recognition*, 2006, pp. 211-216.

[36] A. B. Moreno and A. Sanchez, "GavabDB: A 3D face database," *Proc. Workshop Biometrics on the Internet COST275*, 2004, pp. 77-82.

[37] P.J. Phillips, P.J. Flynn, T. Scruggs, K.W. Bowyer, J. Chang, K. Hoffman, J. Marques, J. Min, and W. Worek, "Overview of the face recognition grand challenge," *Proceedings of the IEEE conference on computer vision and pattern recognition*, 2005, pp. 947-954.

[38] S. Jin, R.R. Lewis, and D. West, "A comparison of algorithms for vertex normal computation," *VISUAL COMPUT.* volume 21, 2005, pp. 71-82.

[39] J. MacQueen, "Some methods for classification and analysis of multivariate observations," *Proc. 5th Berkeley Symp. Mathematical Statistics and Probability*, volume 1, 1967, pp. 281-297.

[40] A.E. Johnson, "Spin-images: A representation for 3-D surface matching," Ph.D. thesis, Robotics Institute, Carnegie Mellon University, 1997.

[41] C.J.C. Burges, "A tutorial on support vector machines for pattern recognition," *DATA MIN. KNOWL. DISC.*, volume 2, 1998, pp. 121-167.

[42] B. Guo, S. Gunn, R. Damper, J. Nelson ,"Customizing kernel functions for SVM-based hyperspectral image classification," *IEEE Transactions on Image Processing.*, vol. 17, no. 4, 2008, pp. 622-629.

[43] C.O. Andrei, "3D affine coordinate transformations," MSc in Geodesy, School of Architecture and the Built Environment, Royal Institute of Technology (KTH), Stockholm, Sweden, 2006.

[44] Y. Hu, M. Zhou, and Z. Wu, "A dense point-to-point alignment method for realistic 3D face morphing and animation," *International Journal of Computer Game Technology*, 2009.

[45] T. Russ, C. Boehnen, T. Peters, "3D face recognition using 3D alignment for PCA," *IEEE Conference on Computer Vision and Pattern Recognition*, pp. 1391–1398, 2006.

Mingli Song (M'06-SM'13)is an Associate Professor in Microsoft Visual Perception Laboratory, Zhejiang University. He received the PhD degree in Computer Science from Zhejiang University, China, in 2006. He was awarded Microsoft Research Fellowship in 2004. His research interests include face modeling and facial expression analysis.

Dacheng Tao (M'07-SM'12) is Professor of Computer Science with the Centre for Quantum Computation & Intelligent Systems and the Faculty of Engineering & Information Technology in the University of Technology, Sydney. He mainly applies statistics and mathematics for data analysis problems in data mining, computer vision, machine learning, multimedia, and video surveillance. He has authored and co-authored 100+ scientific articles at top venues including IEEE T-PAMI, T-NNLS, T-IP, NIPS, ICML, AISTATS, ICDM, CVPR, ICCV, ECCV; ACM T-KDD, Multimedia and KDD, with the best theory/algorithm paper runner up award in IEEE ICDM'07 and the best student paper award in IEEE ICDM'13.

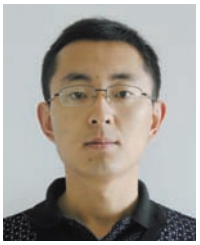

Shengpeng Sun is a Master student in Microsoft Visual Perception Laboratory, Zhejiang University. His research interests include 3D face alignment and facial expression analysis.

Chun Chen is a Professor in the College of Computer Science, Zhejiang University. His research interests include computer vision, computer graphics and embedded technology.

Stephen J. Maybank is a Professor of Department of Computer Science and Information Systems, Birkbeck College, University of London. His research interests include visual surveillance, content based image retrieval, 3D geometry inference, image statistics, etc.. He was awarded the Koenderink Prize at the 10th European Conference on Computer Vision. He is member of the Editorial Board for the International Journal of Computer Vision and Editor for Computing and Informatics. He is Fellow of the IEEE and Fellow of the Royal Statistical Society.